Chinese Chemical Letters 37 (2026) 111188

Contents lists available at ScienceDirect

Chinese Chemical Letters

journal homepage: www.elsevier.com/locate/cclet

In-situ grown high-load single-atom Fe on MoS_2/CFC with super high activity in ammonia synthesis *via* electrochemical nitrate reduction

Lin Xu[a], Lifen Liu[b,*], Guohua Chen[c], Deming Xia[a]

[a] School of Environmental Science and Technology, Dalian University of Technology, Dalian 116024, China
[b] School of Chemical Engineering, Ocean and Life Sciences, Dalian University of Technology, Panjin 124221, China
[c] School of Energy and Environment, City University of Hong Kong, Hong Kong, China

ARTICLE INFO

Article history:
Received 9 October 2024
Revised 10 February 2025
Accepted 8 April 2025
Available online 16 June 2025

Keywords:
Nitrate reduction reaction
Electrocatalytic ammonia synthesis
Single-atom catalysts
Molybdenum disulfide
Binder-free electrode

ABSTRACT

Electrochemically converting nitrate to ammonia under ambient conditions is a hot topic. However, it suffers from low efficiency because of the multi-electron/proton transfer. Herein, high-load atomic Fe (16.45 wt%) *in-situ* grown on carbon fiber cloth (Fe_1@MoS_2/CFC) demonstrates super high activity and selectivity in electrochemical nitrate reduction to ammonia at -0.73 V *vs.* RHE. The maximum NH_3 yield is 28.59 mg h^{-1} cm^{-2}, and the corresponding NH_3-Faradaic efficiency is 96.65% at 360 mA/cm^2 partial current density. The electrode exhibits good durability during ten cycled tests of 1 h each. The X-ray absorption near-edge structure (XANES), extended X-ray absorption fine structure (EXAFS), *in-situ* Raman analysis, and electron paramagnetic resonance (EPR) measurements reveal that the super high activity derives from the rich presence of active sites related to Fe-S and surrounding unsaturated Mo-S. Density functional theory (DFT) calculations show that the atomic Fe facilitates the water dissociation and provides sufficient active hydrogen for the edge Mo to boost nitrate reduction reaction (NO_3^-RR) activity, enhances NH_3 selectivity, and decreases the energy barrier of NH_3 desorption (rate-determining step) by regulating the coordination environment and electronic structure of the active Mo site. This stable and binder-free electrode with high dosage atomic Fe and rich edge Mo active sites is an attractive cathode for NO_3^-RR.

© 2025 Published by Elsevier B.V. on behalf of Chinese Chemical Society and Institute of Materia Medica, Chinese Academy of Medical Sciences.

The commercial high temperature (300-500°C) and pressure (150-200 atm) energy-intensive Haber-Bosch process, a century-old craft for ammonia production, is large scale in global energy consumption (~1% of the annual natural gas) and carbon dioxide emission (at 1.87 ton_{CO2}/ton_{NH3}) [1–4]. Thus formed ammonia is a fundamental chemical in fertilizers and a hydrogen-rich fuel for the next generation [5]. An alternative, using renewable energy for NH_3 synthesis under ambient conditions, is electrochemical nitrogen reduction reaction (NRR) [6–8]. However, the NRR suffers from low Faradaic efficiency (FE) and NH_3 yield due to the limited solubility, high bond energy (N≡N, 941 kJ/mol), and multi-step reductions involving electron/hydrogen [9,10]. The wide use of nitrogen fertilizer caused ground water nitrate pollution. As one of the most widespread nitrogen-containing water-soluble contaminants at varying concentrations (0.001-2 mol/L) in industrial waste streams, nitrate (NO_3^-) has the lower bond energy of N=O (204 kJ/mol), which decreases the reaction energy barrier and increases the NH_3 yield [11,12].

The NO_3^--to-NH_3 conversion is involved in nitrate reduction, as an $8e^-$ transfer process ($NO_3^- + 6H_2O + 8e^- \rightarrow NH_3 + 9OH^-$ in alkaline electrolyte, 0.69 V *versus* the reversible hydrogen electrode (RHE), and a slow process also involving 9 protons [13–16]. The byproducts (NO_2, N_2O, N_2) and competitive hydrogen evolution reaction (HER) affect Faradaic efficiency (FE) and NH_3 yield [17,18]. Therefore, developing catalysts with improved activity, selectivity, and durability remains academically interesting, technically challenging, and industrially demanding.

Single-atom catalysts (SACs) anchor isolated active metal sites by chemically coordinating/bonding them with surrounding atoms from the supports [19]. In atomic dispersion, SACs maximize the use of metals, providing even superior activity than their nanoparticle (NP) counterparts [20–22]. Recently, iron-based SACs have been widely investigated for NO_3^-RR, due to their abundant reserves, low cost, and non-toxic property. Notably, the Haber-Bosch catalysts are also Fe-based [23–26]. According to Wu *et al.* [27], the impressive Fe SACs (max $FE_{NH3} = 75\%$, $Yield_{NH3} = 0.46$ mmol h^{-1} cm^{-2}) isolated Fe-N_4 active sites to prevent the N-N cou-

* Corresponding author.
E-mail address: lifenliu@dlut.edu.cn (L. Liu).

https://doi.org/10.1016/j.cclet.2025.111188
1001-8417/© 2025 Published by Elsevier B.V. on behalf of Chinese Chemical Society and Institute of Materia Medica, Chinese Academy of Medical Sciences.

pling and decrease the thermodynamic barriers compared with Fe NP, Co SAC, and Ni SAC from density functional theory (DFT) calculations. Zhang *et al.* [28] used O atoms to tune the d-center of Fe, making the FeN_2O_2 structure spontaneously trigger the transformation of *NOH to *N, which is the rate-determining reaction based on FeN_4. However, the typical M-C-N type (M = Fe, Co, Cu, Ni …) SACs are limited by linear scaling relations due to the multi-intermediate of the NO_3^-RR [24]. Therefore, tuning the coordination environment is important to boost the performance [29]. Inspired by the composition of the nitrate reductase (containing Fe-S and Mo-S cofactor) [30,31], Murphy *et al.* [32] fabricated a bimetallic FeMo-N-C catalyst and demonstrated that the NO_3^- groups were firstly reduced to NO_2^- by the Mo sites, then the NO_2^- was converted to NH_3 on the Fe sites at 100% FE. Nevertheless, using binders to fix the powder catalysts to the supports, may cover some of the active centers and hinder the efficiency. Molybdenum disulfides (MoS_2), a traditional two-dimensional transition-metal dichalcogenides, can grow firmly on carbon-based conductive substrates, present excellent properties in HER [33], oxygen reduction reaction (ORR) [34] and NRR [35]. Notably, by regulating the defects or doping metals, the effect can be further enhanced [36,37]. Hence, MoS_2-based catalysts grown on carbon substrate are potential binder-free materials for electrochemical NO_3^-RR. In 2022, Li *et al.* [38] supported single iron atoms on MoS_2 nanosheets, showing NO_3^-RR activity. The formed NH_3 yield (431.8 ± 38.6 μg h^{-1} cm^{-2}) was relatively low, but this can be improved by changing the synthesis conditions to adjust the active sites, their coordination environments and loading of Fe SACs.

Herein, we tried to increase the single atom iron loading by an *in-situ* synthesis technique under hydrothermal condition and report the successful preparation of high-loading single atom Fe doped MoS_2 grown on carbon fiber cloth (CFC) for NO_3^-RR, an ultra-high ammonia yield of 28.59 mg h^{-1} cm^{-2} at 360 mA/cm^2 partial current density, with the corresponding NH_3-FE being 96.65% at -0.73 V *vs.* RHE under alkaline conditions. The results outperform the MoS_2/CFC or CFC. The durability in activity and selectivity was excellent, demonstrated by ten times reuse, with one hour in each cycle. The experiments and DFT calculations unveil the synergistic tandem effect of atomic Fe and the surrounding edge Mo sites, indicating that unsaturated Mo is the primary active site for NO_3^- reduction, and atomic Fe is the main active hydrogen donor. Besides, atomic Fe tunes the edge Mo sites' coordination environment and electronic structure to inhibit HER and facilitate NH_3 desorption.

The Fe_1@MoS_2/CFC and MoS_2/CFC catalysts were fabricated by following the same procedures as reported by the authors previously [39]. The preparation details are provided in Supporting information. High-resolution transmission electron microscope (HRTEM), energy-dispersive X-ray spectroscopy (EDS), X-ray diffraction (XRD), X-ray photoelectron spectra (XPS), and X-ray fine structure spectroscopy (XAFS) characterized the microstructure and elemental composition of the Fe_1@MoS_2 on CFC. HRTEM displays that the Fe atoms distribute uniformly in nanoflower-like MoS_2 with 1T and 2H phases (Fig. S1 in Supporting information). The XRD shows that the peaks at 10.9°, 34.7°, and 57.2° belong to the (002), (100), and (110) of MoS_2, while the 25.1° and 43.0° come from the CFC (Fig. S2 in Supporting information) [40–42]. The XPS spectra (Fig. S3 in Supporting information) illustrate that the atomic Fe existed in Fe-S form, suggesting the positive oxidation states of Fe species in Fe_1@MoS_2/CFC, consistent with the XAFS analysis [38]. The content of Fe was 16.45 wt% in Fe_1@MoS_2, tested by inductively coupled plasma optical emission spectrometer (ICP-OES).

The electronic structure and coordination of Fe species in Fe_1@MoS_2/CFC were obtained by the Fe K-edge X-ray absorption near-edge structure (XANES) and extended X-ray absorption fine

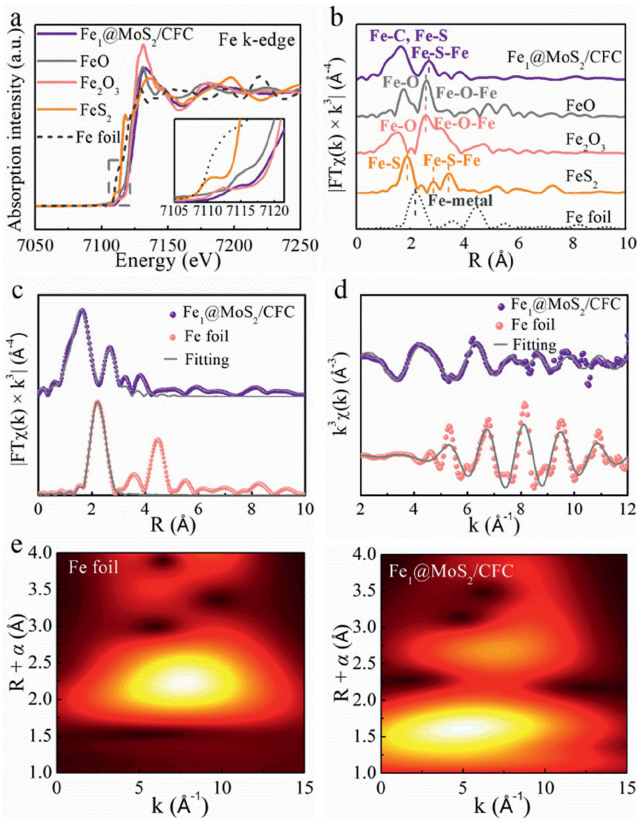


Fig. 1. XAFS characterizations of the Fe_1@MoS_2/CFC. (a) Fe K-edge XANES spectra. (b) FT-EXAFS spectra of Fe. (c, d) EXAFS fitting curve, and (e) Wavelet transforms of EXAFS of the Fe species in Fe_1@MoS_2/CFC and Fe foil.

structure (EXAFS) measurements. Fig. 1a demonstrates that the absorption edge of the sample is located between FeO and Fe_2O_3, illustrating the valence state of Fe is between 2^+ and 3^+ [43,44]. The Fourier transform of EXAFS spectra (FT-EXAFS) (Fig. 1b) exhibits the Fe-S interaction in Fe_1@MoS_2/CFC. No Fe-Fe bands appear at 2.2 Å, suggesting the Fe species are atomically isolated by the surrounding S [45–48]. The coordination number (CN) and geometric configuration were explored by the EXAFS fitting spectra. Figs. 1c and d show the match between the experiments and fitting curves in *R*- and *K*-spaces. The Fe species in Fe_1@MoS_2/CFC have three coordinating interactions at 2.01 Å (with a CN of 5.30), at 2.29 Å (with a CN of 2.40), and 3.05 Å (with a CN of 1.20), corresponding to Fe-C, Fe-S, and Fe-S-Fe, respectively (Table S1 in Supporting information). The wavelet transforms of EXAFS (Fig. 1e) was employed to observe the coordination environment of Fe species in Fe_1@MoS_2/CFC. The maximum intensity appears at ~5.1 $Å^{-1}$, corresponding to Fe-C and Fe-S. No Fe-metal exists, confirming the atomic-level distribution of Fe species [49]. LSV (linear sweep voltammetry) was conducted to investigate the NO_3^-RR activity of Fe_1@MoS_2/CFC in Ar-saturated electrolytes with 1 mol/L KOH. The scan rate for LSV was 5 mV/s. The largest current density was obtained when the concentration of NO_3^- was 0.6 mol/L, and it was enhanced as the magnetic stirring rate up to 500 rpm (Figs. S4 and S5 in Supporting information). The impacts of NO_3^- concentration (0.1, 0.3, 0.6, and 1 mol/L) were further tested. The NH_3 yield rate and FE increased with the NO_3^- concentration from 0.1 mol/L to 0.6 mol/L, while slightly decreasing in 1 mol/L (Fig. S6 in Supporting information), corresponding to the trend observed in Fig. S4. Therefore, we chose 0.6 mol/L and 500 rpm for NO_3^-RR in subsequent tests.

Fig. 2a shows the effect of atomic Fe on NO_3^-RR and comparison of the electrochemical activity of Fe_1@MoS_2/CFC, MoS_2/CFC,

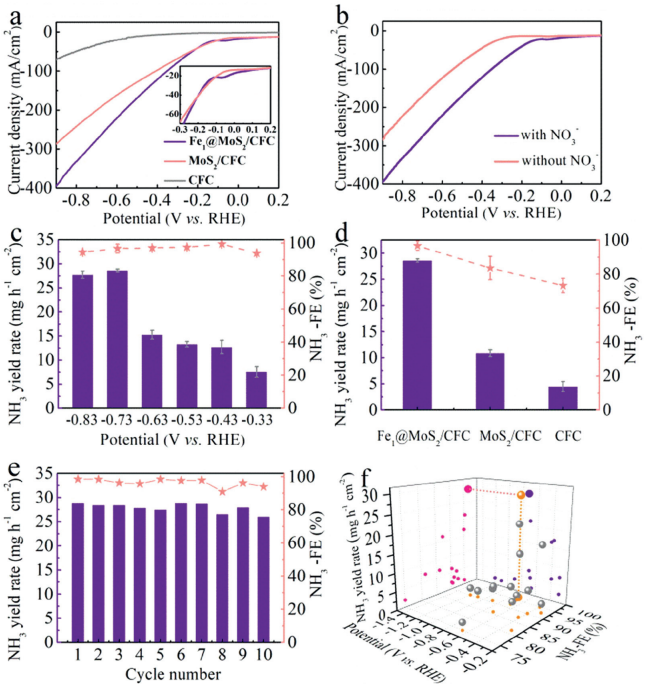


Fig. 2. The electrocatalytic activity for NO_3^-RR in H-cell. (a) LSV curves of Fe_1@MoS_2/CFC, MoS_2/CFC, and CFC in 1 mol/L KOH with 0.6 mol/L KNO_3 (pH 13.5), and (b) Fe_1@MoS_2/CFC in the electrolyte with or without NO_3^-. The scan rate for LSV was 5 mV/s. All reactions were conducted with a magnetic stirring speed of 500 rpm. (c) Potential-dependent FE and yield rate of NH_3 over Fe_1@MoS_2/CFC. (d) The NH_3 yield rate and FE of the Fe_1@MoS_2/CFC, MoS_2/CFC, and CFC at -0.73 V. (e) Durability study of the Fe_1@MoS_2/CFC for 10 hours in 1 mol/L KOH with 0.6 mol/L KNO_3 at -0.73 V. (f) Comparisons of NO_3^-RR performances between Fe_1@MoS_2/CFC (Orange ball) and recently literature-reported catalysts (gray balls).

and CFC. The Fe_1@MoS_2/CFC exhibited an onset potential for nitrate reduction at around 0.06 V, more positive than the MoS_2/CFC (-0.03V), and displayed the largest current density among the three samples. Moreover, in Fig. 2b, without NO_3^-, no activity is observed until -0.25 V, which is the onset of the HER, indicating the suppression of the competitive reaction [50]. According to previous studies, the current peak near 0 V is assigned to the reduction of $^*NO_3$ (adsorbed NO_3^-) to $^*NO_2$, and the peak at around -0.1 V is mainly attributed to the conversion of $^*NO_2$ to $^*NH_3$ [51,52]. Figs. 2a and b demonstrate that the atomic Fe reduced the overpotential of the NO_3^-RR and increased the selectivity of the catalyst for NH_3.

The NO_3^-RR performances of the Fe_1@MoS_2/CFC at different potentials are shown in Fig. 2c. The NH_3 yield rate increased with the potential from -0.33 V to -0.73 V and reached 28.59 mg h^{-1} cm^{-2}, but decreased at more negative potentials due to the competitive HER reaction. Additionally, the Fe_1@MoS_2/CFC showed high NH_3-FE above 93% at -0.33 V to -0.83 V, and the maximum NH_3-FE (99%) at -0.43 V. Notably, the NH_3 yield at 18.07 mg h^{-1} cm^{-2} (Fe_1@MoS_2/CFC) and 90.02% FE in 0.1 mol/L NO_3^-, indicate that it operates effectively with a relatively low NO_3^- concentration (Fig. S6).

The NO_3^-RR activity of the Fe_1@MoS_2/CFC, MoS_2/CFC, and CFC was compared at -0.73 V. Fig. 2d indicates that the NH_3 yield rate and FE of Fe_1@MoS_2/CFC are 2.64 and 1.16 times higher than MoS_2/CFC (10.85 mg h^{-1} cm^{-2}, 83.61%). If pure CFC is used, only 4.48 mg h^{-1} cm^{-2} and 73.27% were obtained. Moreover, the NH_3 partial current density delivered by the Fe_1@MoS_2/CFC, MoS_2/CFC, and CFC were 360 mA/cm^2, 135 mA/cm^2, and 65 mA/cm^2, respectively (Fig. S7 in Supporting information). Fig. 2d and Fig. S7 demonstrate that the atomic Fe promoted activity and selectivity to the NO_3^-RR. The content of Fe in the Fe_1@MoS_2/CFC increased with the corresponding ion concentrations in the precursor as expected (Table S2 in Supporting information). Besides, the yield rate and FE of NH_3 improved with the Fe ion precursor concentration from 0.005 mol/L to 0.04 mol/L, due to the more abundant active sites (Fig. S8 in Supporting information). With the absence of nitrate ions or external potential, only very little ammonia was produced (<0.2 mg h^{-1} cm^{-2}), confirming that the NH_3 was mainly synthesized *via* the electrocatalytic NO_3^-RR process (Fig. S9 in Supporting information). The durability was tested by repeating ten times of experiments each operating in 1 h. Fig. 2e shows that Fe_1@MoS_2/CFC has insignificant decreases in NH_3 yield (-9.6%) and FE (-4.7%). The NO_3^-RR performance is compared with the recent reports in Fig. 2f (more details can be found in Table S3 in Supporting information). The Fe_1@MoS_2/CFC has superior NH_3 yield and FE, due to the binder-free electrode being advantageous for its good stability, low-cost, and numerous exposed active sites.

In-situ Raman spectra of Fe_1@MoS_2/CFC and MoS_2/CFC at various applied potentials during the NO_3^-RR are displayed in Figs. 3a and b, respectively. The peak at 1049 cm^{-1} is associated with symmetric stretching of NO_3^-, suggesting the $^*NO_3$ on the surface of the electrodes [53]. The Raman bands at around 1300 cm^{-1} and 1600 cm^{-1} are attributed to the D and G bands of the carbon substrates [54]. The weak signal that appears at 819 cm^{-1} is ascribed to Mo_2-O vibration because of the partial oxidation of Mo species under the laser, consistent with the characteristic peak of the electrodes (Figs. S10 and S11 in Supporting information) [55]. In Fig. 3a, the peak at 670 cm^{-1} demonstrated that the partial atomic Fe in Fe_1@MoS_2/CFC exists as the ferric iron species in alkaline solutions [56]. The peak intensity decreased with the applied reduction potential at 0.2 V to 0 V, indicating that the ferric iron species is reducing to a relatively low chemical state by external electricity. However, when the potential shifts to more negative, the characteristic peak increases again, suggesting that the low chemical state Fe is oxidized to Fe^{3+} again, indicating that atomic Fe participated in the reaction and Fe_1@MoS_2/CFC had dynamic stability [57].

To unveil the role of atomic Fe and NO_3^-RR mechanism, the Gibbs free energy of water dissociation and NO_3^--to-NH_3 pathway with deoxidation ($^*NO_3 \rightarrow {}^*NO_2 \rightarrow {}^*NO \rightarrow {}^*N$) and hydrogenation ($^*N \rightarrow {}^*NH \rightarrow {}^*NH_2 \rightarrow {}^*NH_3$) were calculated using DFT, under a potential of 0 V and pH 13.5 (Figs. 3c-f) [58,59]. The adsorption configurations of different intermediates on the Fe/Mo site of Fe_1@MoS_2 and MoS_2 are provided (Figs. S12-S17 in Supporting information).

Figs. 3d and e show that the adsorption energy of $^*NO_3$ (ΔG_{NO3}) on the Mo site is more robust than Fe, demonstrating that unsaturated Mo on the edge of Fe_1@MoS_2 is thermodynamically more favorable to NO_3^-RR. Meanwhile, the ΔG_{NO3} (-1.804 eV) on Mo site in Fe_1@MoS_2 is higher than ΔG_{H2O} (-0.32 eV), indicating that NO_3^- is more easily adsorbed on Mo site than H_2O and explaining the high selectivity of Fe_1@MoS_2 for NO_3^-RR (Fig. 3c) [60,61]. Similarly, we found water splitting on atomic Fe priority by comparing the ΔG_{NO3} (-0.668 eV) and ΔG_{H2O} (-0.782 eV). Moreover, Fig. 3c shows that the Mo site has an extraordinary adsorption ability for active hydrogen ($^*H$), promoting the HO-H cleaving on the surrounding Fe sites [62]. Furthermore, for the competitive HER, the Mo site in Fe_1@MoS_2 has the most stable ΔG_H to suppress the H_2 formation [63].

EPR spectroscopy probes that the Fe_1@MoS_2/CFC exhibits the strongest DMPO-H signals with high $^*H$ formation capacity in the electrolyte without NO_3^- (Fig. S18 in Supporting information). In the presence of NO_3^-, the DMPO-$^*H$ signals surrounding Fe_1@MoS_2/CFC are hardly detected, indicating that the $^*H$ is consumed quickly by NO_3^-RR. However, for MoS_2/CFC, the DMPO-$^*H$

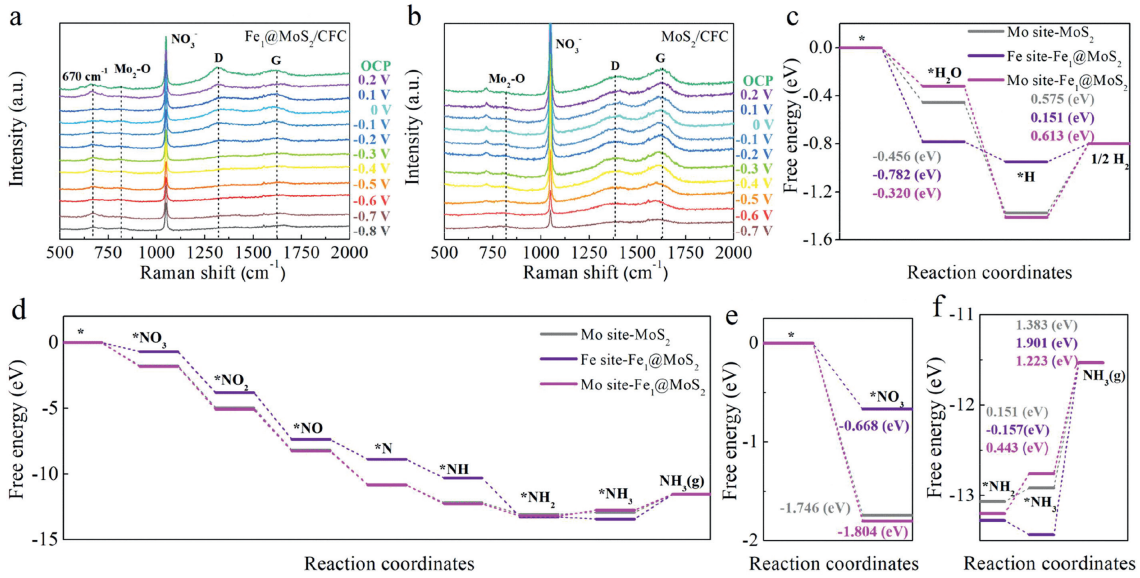


Fig. 3. *In-situ* Raman spectra of (a) $Fe_1@MoS_2$/CFC and (b) MoS_2/CFC during the NO_3^-RR at different potentials in a solution with 1 mol/L KOH and 0.6 mol/L KNO_3. Free energy diagrams for (c) water splitting and (d) NO_3^-RR on the metal atom sites in $Fe_1@MoS_2$ and MoS_2. (e, f) The enlargement of the details in the NO_3^-RR diagram.

still exists, representing a sluggish reaction rate (Fig. S19 in Supporting information) [64].

From the overall NO_3^-RR steps displayed in Figs. 3d-f, the Mo site in $Fe_1@MoS_2$ has the most vigorous $^*NO_3$ adsorption energy and lowest NH_3 desorption energy barrier, the rate-determining step (RDS), compared with the pure MoS_2 [65,66]. In addition, the rapid electron transfer efficiency and fast reaction kinetics of $Fe_1@MoS_2$/CFC were identified by their smaller Tafel slope of 321 mV/dec than those of MoS_2/CFC (341 mV/dec) and CFC (497 mV/dec) (Fig. S20 in Supporting information) [67].

Therefore, the crucial function of atomic Fe has been summarized: (1) enhancing the H_2O adsorption and supplying sufficient active hydrogen for the Mo site to accelerate the NO_3^-RR [67,68]; (2) regulating the coordination environment and electronic structure of the surrounding Mo atom, thereby enhancing the adsorption capacity of the $^*NO_3$ and partial nitrogen-containing intermediates, making NH_3 desorption easier, and promoting the reactivation of the active sites.

The *in-situ* grown catalysts, the high-load atomic Fe in MoS_2 on CFC, show superior electrocatalytic NO_3^-RR activity for ammonia synthesis under ambient conditions. Using $Fe_1@MoS_2$/CFC, at a rate of 28.59 mg h^{-1} cm^{-2}, NH_3 is formed, 96.65% FE_{NH3} at -0.73 V. The electrode has good durability with insignificant degradation after ten repeated times. The synergistic tandem effect of atomic Fe and surrounding Mo edge sites boosted the NO_3^-RR performance in activity and selectivity because of the adequate supply of active hydrogen, enhanced electron transfer, increased nitrate adsorption, and decreased free energy of ammonia desorption, making it promising in future applications in ammonia synthesis.

Declaration of competing interest

The authors declare that they have no known competing financial interests or personal relationships that could have appeared to influence the work reported in this paper.

CRediT authorship contribution statement

Lin Xu: Writing – review & editing, Writing – original draft, Validation, Methodology, Investigation, Formal analysis, Conceptualization. **Lifen Liu:** Writing – review & editing, Validation, Supervision, Resources, Project administration, Methodology, Funding acquisition, Formal analysis, Conceptualization. **Guohua Chen:** Writing – review & editing, Supervision, Software, Methodology, Formal analysis. **Deming Xia:** Data curation, Software, Visualization.

Acknowledgments

This work was supported by grant project (No. 22276026) from National Natural Science Foundation of China. We thank Prof. Minghuui Yang in Dalian University of Technology for his kind assistance in in-situ Raman analysis.

Supplementary materials

Supplementary material associated with this article can be found, in the online version, at doi:10.1016/j.cclet.2025.111188.

References

[1] Y. Cui, A. Dong, Y. Zhou, et al., Small 19 (2023) 2207661.
[2] W. Chen, X. Yang, Z. Chen, et al., Adv. Funct. Mater. 33 (2023) 2300512.
[3] S. Dong, A. Niu, K. Wang, et al., Appl. Catal. B 333 (2023) 122772.
[4] S.L. Foster, S.I.P. Bakovic, R.D. Duda, et al., Nat. Catal. 1 (2018) 490–500.
[5] W. He, J. Zhang, S. Dieckhöfer, et al., Nat. Commun. 13 (2022) 1129.
[6] S. Zhang, M. Han, T. Shi, et al., Nat. Sustain. 6 (2023) 169–179.
[7] Y.X. Lin, S.N. Zhang, Z.H. Xue, et al., Nat. Commun. 10 (2019) 4380.
[8] S. Liu, T. Qian, M. Wang, et al., Nat. Catal. 4 (2021) 322–331.
[9] F.Y. Chen, Z.Y. Wu, S. Gupta, et al., Nat. Nanotechnol. 17 (2022) 759–767.
[10] Y. Wang, S. Wang, Y. Fu, et al., Chin. J. Catal. 56 (2024) 104–113.
[11] E. Murphy, B. Sun, M. Rüscher, et al., Adv. Mater. 36 (2024) 2401133.
[12] K. Chen, D. Ma, Y. Zhang, et al., Adv. Mater. 36 (2024) 2402160.
[13] K. Fan, W. Xie, J. Li, et al., Nat. Commun. 13 (2022) 7958.
[14] R. Jia, Y. Wang, C. Wang, et al., ACS Catal. 10 (2020) 3533–3540.
[15] R. Chen, S. Shen, K. Wang, et al., Proc. Natl. Acad. Sci. U. S. A. 120 (2023) e2312550120.
[16] Y. Liu, X. Zhao, C. Long, et al., Chin. J. Catal. 52 (2023) 196–206.
[17] J. Li, G. Zhan, J. Yang, et al., J Am. Chem. Soc. 142 (2020) 7036–7046.
[18] S. Garcia-Segura, M. Lanzarini-Lopes, K. Hristovski, P. Westerhoff, Appl. Catal. B 236 (2018) 546–568.
[19] A. Wang, J. Li, T. Zhang, Nat. Rev. Chem. 2 (2018) 65–81.
[20] Y. Ren, Y. Tang, L. Zhang, et al., Nat. Commun. 10 (2019) 4500.
[21] F. Chen, X.-L. Wu, C. Shi, et al., Adv. Funct. Mater. 31 (2021) 2007877.
[22] Y. Jiang, J. Yang, M.-L. Li, et al., Chin. J. Catal. 59 (2024) 195–203.
[23] C. Wang, Y. Zhang, H. Luo, et al., Small Methods 6 (2022) 2200790.
[24] S. Zhang, J. Wu, M. Zheng, et al., Nat. Commun. 14 (2023) 3634.
[25] S. Zhang, M. Li, J. Li, Q. Song, X. Liu, Proc. Natl. Acad. Sci. U. S. A. 119 (2022) e2115504119.
[26] C. Liu, G. Zhang, W. Zhang, Z. Gu, G. Zhu, Proc. Natl. Acad. Sci. U. S. A. 120 (2023) e2209979120.

[27] Z.-Y. Wu, M. Karamad, X. Yong, et al., Nat. Commun. 12 (2021) 2870.
[28] W.-D. Zhang, H. Dong, L. Zhou, et al., Appl. Catal. B 317 (2022) 121750.
[29] A. Khorshidi, J. Violet, J. Hashemi, A.A. Peterson, Nat. Catal. 1 (2018) 263–268.
[30] V. Fourmond, M. Sabaty, P. Arnoux, et al., J. Phys. Chem. B 114 (2010) 3341–3347.
[31] C. Sparacino-Watkins, J.F. Stolz, P. Basu, Chem. Soc. Rev. 43 (2014) 676–706.
[32] E. Murphy, Y. Liu, I. Matanovic, S. Guo, et al., ACS Catal. 12 (2022) 6651–6662.
[33] J. Zhang, J. Wu, H. Guo, et al., Adv. Mater. 29 (2017) 1701955.
[34] I.S. Amiinu, Z. Pu, X. Liu, et al., Adv. Funct. Mater. 27 (2017) 1702300.
[35] L. Zhang, X. Ji, X. Ren, et al., Adv. Mater. 30 (2018) 1800191.
[36] S. Jiao, Z. Yao, F. Xue, et al., Appl. Catal. B 258 (2019) 117964.
[37] J. Ge, D. Zhang, Y. Qin, et al., Appl. Catal. B 298 (2021) 120557.
[38] J. Li, Y. Zhang, C. Liu, et al., Adv. Funct. Mater. 32 (2022) 2108316.
[39] L. Xu, L. Liu, Appl. Catal. B 304 (2022) 120953.
[40] X. Li, G. Zhang, Y. Chang, et al., Chem. Eng. J. 499 (2024) 156337.
[41] X. Chen, R. Pan, H. Xu, et al., Appl. Catal. B 361 (2025) 124688.
[42] M.K. Kim, B. Lamichhane, B. Song, et al., Appl. Catal. B 352 (2024) 124037.
[43] X. Sun, Y. Qiu, B. Jiang, et al., Nat. Commun. 14 (2023) 291.
[44] J. Xu, S. Zhang, H. Liu, et al., Angew. Chem. Int. Ed. 62 (2023) e202308044.
[45] W. Wan, Y. Zhao, S. Wei, et al., Nat. Commun. 12 (2021) 5589.
[46] Z. Jin, P. Li, Y. Meng, et al., Nat. Catal. 4 (2021) 615–622.
[47] Y. Sun, R. Li, C. Song, et al., Appl. Catal. B 298 (2021) 120537.
[48] Y. Yan, S. Liang, X. Wang, et al., Proc. Natl. Acad. Sci. U. S. A. 118 (2021) e2110036118.
[49] K. Chen, J. Wang, J. Kang, et al., Appl. Catal. B 324 (2023) 122241.
[50] A. Paliwal, C.D. Bandas, E.S. Thornburg, R.T. Haasch, A.A. Gewirth, ACS Catal. 13 (2023) 6754–6762.
[51] Y.Y. Lou, Q.Z. Zheng, S.Y. Zhou, et al., ACS Catal. 14 (2024) 5098–5108.
[52] Y. Liu, J. Ma, S. Huang, S. Niu, S. Gao, Nano Energy 117 (2023) 108840.
[53] Z. Gu, Y. Zhang, Y. Fu, et al., Angew. Chem. Int. Ed. 63 (2024) e202409125.
[54] C. Wang, K. Li, M. Zhao, Z. Li, J. Zheng, Sep. Purif. Technol. 340 (2024) 126641.
[55] N. Pu, A. Hu, Q. Yang, et al., Chem. Eng. J. 499 (2024) 156100.
[56] X. Lv, Y. Li, F. Deng, et al., Chem. Eng. J. 475 (2023) 146128.
[57] X. Shi, M. Xie, K. Yang, et al., Angew. Chem. Int. Ed. 63 (2024) e202406750.
[58] S. Xu, Y. Shi, Z. Wen, et al., Appl. Catal. B 323 (2023) 122192.
[59] N. Zhou, Z. Wang, N. Zhang, et al., ACS Catal. 13 (2023) 7529–7537.
[60] K. Chen, G. Wang, Y. Guo, D. Ma, K. Chu, Nano Res. 16 (2023) 8737–8742.
[61] Z. Zhang, Y. Liu, X. Su, et al., Nano Res. 16 (2023) 6632–6641.
[62] L. Xiao, C. Cheng, T. Yang, et al., Adv. Mater. 36 (2024) 2411134.
[63] Y. Zhu, K. Fan, C.-S. Hsu, et al., Adv. Mater. 35 (2023) 2301133.
[64] S. Luo, H. Guo, T. Li, et al., Appl. Catal. B 351 (2024) 123967.
[65] H. Lin, J. Wei, Y. Guo, et al., Adv. Funct. Mater. 34 (2024) 2409696.
[66] D. Wu, K. Chen, P. Lv, et al., Nano Lett. 24 (2024) 8502–8509.
[67] Y. Wang, F. Hao, M. Sun, et al., Adv. Mater. 36 (2024) 2313548.
[68] G. Zhang, X. Li, K. Chen, et al., Angew. Chem. Int. Ed. 62 (2023) e202300054.